PCCP

Accepted Manuscript

ROYAL SOCIETY OF CHEMISTRY

www.rsc.org/pccp

for submission to *Physical Chemistry Chemical Physics*

Ceria-based Electrospun Fibers for Renewable Fuel Production via Two-Step Thermal Redox Cycles for Carbon Dioxide Splitting

William T. Gibbons[a], Luke J. Venstrom[b], Robert M. De Smith[c], Jane H. Davidson[c,+], Gregory S. Jackson[d,+]

[a] Department of Chemical Engineering, University of Maryland, College Park, MD 20742; U.S.A.

[b] Department of Mechanical Engineering Valparaiso University, Valparaiso, IN 46383; U.S.A

[c] Department of Mechanical Engineering, University of Minnesota, Minneapolis, MN 55455; U.S.A.

[d] Department of Mechanical Engineering, Colorado School of Mines, Golden, CO 80401; U.S.A.

+ Corresponding authors contact:
email: gsjackso@mines.edu
phone: 1-303-273-0409
email: jhd@umn.edu
phone: 1-612-626-9850

Abstract

Zirconium-doped ceria ($Ce_{1-x}Zr_xO_2$) was synthesized through a controlled electrospinning process as a promising approach to cost-effective, sinter-resistant material structures for high-temperature, solar-driven thermochemical redox cycles. To approximate a two-step redox cycle for solar fuel production, fibrous $Ce_{1-x}Zr_xO_2$ with relatively low levels of Zr-doping ($0 < x < 0.1$) were cycled in an infrared-imaging furnace with high-temperature (up to 1500 °C) partial reduction and lower-temperature (~ 800 °C) reoxidation via CO_2 splitting to produce CO. Increases in Zr content improve reducibility and sintering resistance, and, for $x \leq 0.05$, do not significantly slow reoxidation kinetics for CO production. Cycle stability of the fibrous $Ce_{1-x}Zr_xO_2$ (with $x = 0.025$) was assessed for a range of conditions by measuring rates of O_2 release during reduction and CO production during reoxidation and by assessing post-cycling fiber crystallite sizes and surface areas. Sintering increases with reduction temperature but occurs primarily along the fiber axes. Even after 108 redox cycles with reduction at 1400 °C and oxidation with CO_2 at 800 °C, the fibers maintain their structure with surface areas of ~0.3 m^2/g, higher than those observed in the literature for other ceria-based structures operating at similarly high temperature conditions. Total CO production and peak production rate stabilize above 3.0 mL g^{-1} and 13.0 mL min^{-1} g^{-1}, respectively. The results show the potential for electrospun oxides as sinter-resistant material structures with adequate surface area to support rapid CO_2 splitting in solar thermochemical redox cycles.

Broader Context (200 words):

The use of concentrated sunlight to drive endothermic CO_2 splitting at high temperature is a promising path to the efficient storage of solar energy in chemical form. A two-step thermochemical cycle reduces temperature requirements, simplifies separation issues for CO_2

and/or H_2O splitting, and can provide the basis for renewable fuel or other hydrocarbon production. Such cycles require a working material capable of rapid and reversible reduction and oxidation, and CeO_2-based oxides have received much interest. It is necessary to provide some structure in a cost-effective and scalable manner to the CeO_2-based material with sufficient surface area for adequately fast CO_2 splitting. Electrospinning is a process capable of producing CeO_2-based (or other ceramic) fibers that retain adequate surface area despite exposure to intense operating conditions in the simulated solar-driven, high-temperature redox cycles.

Introduction

Solar-driven thermal redox cycles offer the potential for efficient storage of intermittent solar energy and for production of renewable fuels compatible with the existing transportation fueling infrastructure.[1] Two-step, temperature-swing redox cycles include a high temperature reduction step in which concentrated solar energy drives the endothermic reduction of an oxide material, and a lower temperature step in which the reduced material is reoxidized with CO_2 and/or H_2O to produce CO and/or H_2. The CO and H_2 can be further processed to liquid fuel. Many researchers have studied metal/metal oxide pairs, such as Zn/ZnO or Sn/SnO, but these redox cycles require rapid quenching of the reduced volatile metals to avoid recombination in the first step.[1-4] For this reason, partially reducible oxides with multivalent cations have been proposed as an alternative basis for redox cycles. Ferrite-based cycles avoid the volatility issues of metal/metal oxide cycles, but they suffer from relatively slow kinetics exacerbated by extensive sintering at reduction temperatures of > 1400 °C.[5, 6] In recent years, ceria (CeO_2)-based cycles have received significant attention because of their potential for stable cycling and favorable $CeO_{2-\delta}$ reoxidation kinetics, but they too require high reduction temperatures and efforts to find sinter-resistant structures and materials compositions remain a challenge.[7-10]

The overall reactions for ceria-based solar-driven cycles are as follows:

$$CeO_2 \rightarrow CeO_{2-\delta} + 0.5\cdot\delta\cdot O_2 \qquad \text{(R1)}$$

$$CeO_{2-\delta} + \delta\cdot CO_2 \rightarrow CeO_2 + \delta\cdot CO \qquad \text{(R2)}$$

$$CeO_{2-\delta} + \delta\cdot H_2O \rightarrow CeO_2 + \delta\cdot H_2 \qquad \text{(R3)}$$

To achieve high degrees of reduction ($\delta \rightarrow 0.05$), reaction R1, which is endothermic, requires temperatures at 1400 °C or higher depending on the oxygen partial pressure (P_{O2}).[11-13] The exothermic reoxidation reactions R2 and/or R3 are thermodynamically favored at lower

temperatures (< 1000 °C) where, at reasonable concentrations of CO_2 and/or H_2O, negative free energies of reaction can drive the reaction to near completion. While thermodynamically favored at lower temperatures, reactions R2 and R3 require temperatures above ~700 °C to attain favorable rates of CO and H_2 production.[7, 9, 14] Rapid production of CO and/or H_2 also requires ceria structures featuring high surface area because the rate of ceria reoxidation is limited by surface kinetics rather than the chemical diffusion of oxygen in the ceria lattice.[7, 15, 16] The need for surface area to promote rapid rates of H_2 and CO production presents a challenge for ceria-based, solar-driven redox cycles because the high temperatures required for the reduction of ceria lead to sintering and corresponding loss of surface area.

Many research groups have explored thermochemical cycling and stability of undoped- and doped-ceria structures with initially high surface areas. Chueh et al. used a sacrificial pore former to produce pressed CeO_2 pellets with as high as 65% porosity, but collapse of the porous structure after sintering at 1500 °C led to surface areas of no more than 0.1 $m^2\ g^{-1}$.[7] In later work by the same authors, porous monolithic CeO_2 was produced with 80% initial porosity by a similar sacrificial pore former approach.[17] Long-term cycling of the monoliths with reduction temperatures of 1500 °C led to grain growth and faceting and to an associated drop in fuel (H_2) production rates from ~ 3.0 to 1.5 mL $min^{-1}\ g^{-1}$ when averaged over the period to reach 90% reoxidation. Slow fuel production rates for ceria-based thermochemical cycles encourage further exploration of alternative high-surface-area structures.

Rudisill et al. showed that CeO_2 3-D ordered macro-porous (3DOM) structures, with surface areas of 4 $m^2\ g^{-1}$ after repeated reduction at 1200 °C, increased fuel production rates by 10 times over commercial CeO_2 powders.[15] The 3DOM structures, however, were not cycled at higher temperatures thermodynamically necessary for higher specific fuel production due to dramatic

loss of pore structure and surface area above 1200 °C. Furler et al. tested reticulated porous and commercial felt CeO_2 (with fiber diameters of 4-6 μm), but cyclic testing of both structures with reduction above 1500 °C and reoxidation with H_2O/CO_2 over a range of temperatures as the reactor cooled from 1300 to 500 °C yielded mean rates of H_2 + CO production less than 0.2 mL min^{-1} g^{-1}.[9,18] Moreover, the slow reoxidation rates significantly lower solar-to-fuel efficiency due to the excessive requirement for heating of unutilized oxidant flows.

To achieve faster oxidation rates and greater fuel production, some researchers have focused on using doped ceria to mitigate sintering and lower the required reduction temperature in order to improve the stabilized specific surface area. Some of the most promising dopants to improve ceria reducibility have included tetravalent Zr [19-22] and Hf [22], trivalent Sc [22, 23] and Pr [24], and combinations of Zr with trivalent dopants such as Gd.[21] Preferred dopants such as Zr at levels of 10 mol% or higher have been shown to mitigate sintering and to increase the extent of reduction.[25-30] According to computational studies using density functional theory, Zr-doping improves reduction of ceria by lowering the energy barrier for oxide ion transport to the surface and enhances the production of oxygen vacancies and reduced ceria.[31] However, at dopant levels of 10 mol% or more, these dopants significantly slow rates of reoxidation with either H_2O or CO_2 compared to undoped ceria such that it becomes difficult in thermochemical cycling to recover the full extent of reduction.[22, 24, 27] On the other hand, lower levels of doping have shown promise at balancing the tradeoff between achieving increased reducibility while retaining the rapid oxidation rates of undoped CeO_2.[22] Lee et al. explored reoxidation rates of Zr- and Sc-doped ceria powders and reported that low levels of 3 – 10 % Sc-doping provided a favorable combination of high reducibility at 1500 °C and reoxidation rates with H_2O at 500 °C, which were more than twice that of undoped CeO_2.[23] These results are inconsistent with Scheffe et al.

who reported that Zr- and Hf-doping below 10% were superior to Sc-doping at the same levels in terms of cyclic reducibility data for doping levels of 10% or lower[22]. In general, many questions remain about the effectiveness of low levels of Zr-doping and its effect on high-temperature reduction and reoxidation rates with H_2O and/or CO_2, and these open questions motivated the choice of material compositions in this paper.

This study assesses the potential of cost-effective electrospun ceria-based fibers for maintaining surface areas and adequately small grain sizes necessary for good reduction and fast lower temperature reoxidation in solar-driven redox cycles. Electrospun structures can potentially provide high surface area to accelerate the low-temperature reoxidation surface kinetics and sustain structures that mitigate sintering at high reduction temperatures. Electrospinning of cation salts with subsequent oxidation can produce ceramic fibers with diameters ranging from 2 μm down to 100 nm.[32] Electrospun ceramics can produce non-woven structures or mats with limited fiber entanglement [33] and such structures are shown to restrict material sintering primarily to along the axis of the fibers. If electrospun structures mitigate sintering at the high temperatures needed for the proposed thermochemical cycles, electrospinning will be a promising synthesis route to explore for ceria-based structures to meet the challenges of high-temperature, solar-driven redox cycles. In this study, pure and Zr-doped CeO_2 fibers ($Ce_{1-x}Zr_xO_2$, where x = 0.0, 0.025, 0.05, 0.10) are synthesized and characterized to determine the viability of spun fibers as working material structures for solar thermal applications for reduction temperatures up to 1500 °C.

Experimental Approach

Electrospun Fiber Synthesis

To produce the electrospun ceramic fibers, soluble hydrated-salt precursors are added to a viscous polymer solution to produce a homogenous viscous solution suitable for electrospinning. A stock solvent solution was created from 200 g dimethylformamide (DMF), 200 g anhydrous ethanol, and 50 g deionized water. The solution was combined with 60 g polyvinylpyrolidone (PVP, MW = 1.3 x 10^6 Alpha Aesar) to form an 11.7 wt.% PVP solution. The viscous polymer solution was kept tightly capped and sonicated for at least 12 hr to fully dissolve the granular PVP.

For the Ce and Zr precursor solution, $Ce(NO_3)_3 \bullet 6H_2O$ (Alpha Aesar) and $ZrO(NO_3)_2 \bullet 6H_2O$ (Alpha Aesar), were dissolved in a small volume of the same stock solvent (200 g DMF, 200 g ethanol, 50 g H_2O) to yield a solution with the desired Ce:Zr ratio. The Ce and Zr precursor solution was then added to the stock polymer solution. For example, to produce the $Ce_{0.975}Zr_{0.025}O_2$ sample, 4.889 g of $Ce(NO_3)_3 \bullet 6H_2O$ and 0.0979 g of $ZrO(NO_3)_2 \bullet 6H_2O$ were combined in a 10 mL centrifuge tube with 10 mL of the stock solvent solution and sonicated for 30 minutes. The solution containing the dissolved metal salts was then added to 40 mL of the stock PVP solution and sonicated for 30 min to form a homogenous, viscous spinning solution. This solution was then poured into the spinning solution trough as illustrated in the system diagram in Figure 1.

As shown in Figure 1, the electrospinning process involves the use of a spinneret on which drops of viscous polymeric solution containing the ceramic precursors are produced on a wire coil rotating through the bath of spinning solution.[34] The drops are subjected to a high-strength electric field (~1-2 kV/cm) created between the spinneret and a collector. The charge concentration on the surface of the drop of solution is of such magnitude that the electrostatic forces overcome surface tension and form a jet of solution, which is propelled in a thin

continuous stream to a collector. As the jet travels, it experiences solvent evaporation and stretching/thinning. This method produces textile-like non-woven sheets of fibers at the collector, and offers control over production rates, composition, fiber diameter, and fiber morphology by varying electric field strength and spinning solution composition.

For this study, a copper-wire coil spinneret (with coil spacing = 1 cm, coil diameter = 2.5 cm) fixed to a metal shaft was rotated through the spinning solution at 30 rpm. A high voltage power supply (Spellman FJ60) was used in constant current mode (current limit = 0.15 mA) to apply a voltage of 25 +/- 2 kV to the wire coil spinneret while another high voltage power supply (Spellman, model CZE1000R) was used to fix a second rotating wire drum collector at potential of -10 kV. The negative voltage on the collector eliminated fibers finding undesirable grounds and thereby improved the fiber collection efficiency. The collector (diameter = 10 cm) rotated at 300 rpm. The spinneret to collector distance was fixed at 15 cm, thereby creating an electric field of 2 kV/cm during the entire spinning process.

Heated air was blown across the fibers to ensure favorable drying conditions while minimizing solvent evaporation from the spinning solution trough. The spinning solution was replenished at 10 minute intervals and sheets of fibers removed from the collector at 20 minute intervals. Each batch required ~60 minutes to spin, and yielded 4-5 g spun fibers (pre-polymer removal). Spun fibers were stored in a heated glassware oven (90 °C, < 7.5% RH at all times) to minimize fiber welding caused by high relative humidity.[35]

To complete the synthesis, the polymer and the anions of the Ce/Zr salts from the fibrous material were removed by heating in air at 2 °C min^{-1} to 150 °C and holding at 150 °C for 3 h to evaporate the solvents. The material was heated at 0.1 °C min^{-1} to 300 °C and held at 300 °C to decompose the polymer slowly. Finally, the fibers were heated to 550 °C at 2 °C min^{-1} and

maintained at 550 °C for 3 h to complete the decomposition of the precursor materials and to complete the oxidation of the remaining Ce and Zr to produce flexible sheets of ceramic fibers. The final yield for each batch was 1.5 ± 0.2 g depending on fiber collection efficiency.

Characterization

To evaluate the effects of the redox cycling on the fiber structure, crystallite size and surface area, scanning electron microscopy (SEM), surface area measurements with Kr-adsorption, and X-ray diffraction (XRD) were carried out on both post-processed and post-cycled samples. Fibers before and after testing were characterized via SEM in a Hitachi SU-70 SEM with a 10 kV accelerating voltage and a working distance of 10 mm. Before imaging, a conductive Au/Pd alloy layer was sputtered on to the samples to reduce charging. Surface area measurements were conducted using a Micromeretics ASAP 2020, with Kr as the adsorbate. Samples were degassed for 3 h at 300 °C before analysis. Adsorption measurements were conducted over the range P/P^0 = 0.01-0.30 at 350 °C, and surface areas were calculated with the Brunauer–Emmett–Teller (BET) model.[36]

XRD patterns for tested samples were recorded with a Bruker D8 advance diffractometer (Cu Kα radiation, λ = 0.15418 nm) over a 2θ range of 20-90°. Each diffraction pattern exhibits the fluorite structure, and no evidence of phase segregation was found, which is consistent with the extensive automotive catalyst literature involving Zr doped CeO_2.[37-39] Diffraction patterns were analyzed via Rietveld refinement to determine the lattice parameter for each sample. A linear relationship exists between the Zr concentration and the cubic lattice parameter, as expected by Vegard's Law for the formation of solid solutions[40], and the diffraction peaks shift to larger angles 2θ as the Zr content increases. In addition, broadening of the diffraction peaks as found

from Rietveld refinement was used to determine the decrease in average crystallite size with increased Zr content.

Thermochemical Cycling

To test the redox activity and stability of the electrospun $Ce_{1-x}Zr_xO_2$, 0.3 g of material was packed into a 9.5-mm diameter, 5-cm long porous bed with an initial porosity of ca. 98%. This correlates to a bed density of approximately 0.09 g cm^{-3} which is approximately half the initial fiber bed density for the commercial ceria fiber redox tests in Furler et al.[12]. The porous bed was held in an alumina tube and cycled between reduction and oxidation temperatures and gas atmospheres in an IR imaging furnace (Ulvac-Riko, VHT-E44). An alumina-shielded Pt/Pt-Rh thermocouple was inserted into the center of the fiber bed to monitor its temperature and a second unshielded Pt/Pt-Rh thermocouple was placed downstream of the fibers as input to the PID controller of the furnace. Reducing and oxidizing gas flows were controlled via mass flow controllers and pneumatically actuated solenoid valves to generate step changes between reducing and oxidizing atmospheres. During reduction, the gas consisted of 10 ppm O_2 (P_{O2} = 10^{-5} bar) in a background of N_2 flowing at 300 mL min^{-1}, and during oxidation, the gas consisted of 25 mol% CO_2 in a background of N_2 flowing at 400 mL min^{-1}.

The sample was first heated under the reducing gas flow from 25 °C to 500 °C at 20 °C min^{-1} to protect the alumina tube from thermal shock, and then ramped at 100 °C min^{-1} to the reduction temperature (T_{red}) specified for each test. The reduction temperature was held for 1 h to stabilize the fibers in preparation for cycling. The sample was then cooled to a reoxidation temperature (T_{ox}) of 800 °C at 200 °C min^{-1} and held at T_{ox} for 2 min. For most tests, ten thermochemical cycles were then executed sequentially. A single cycle consisted of a 100 °C min^{-1} ramp to T_{red}, a dwell at T_{red} for 5 min, cooling at 200 °C min^{-1} to T_{ox}, injection of CO_2 for 4 min for oxidation,

and a 2 min purge at T_{ox} in the reducing gas flow. Gas composition at the inlet and outlet was monitored once every second using an in-line Raman laser gas analyzer (Atmosphere Recovery Inc. Model 129a) with a detectable limit of 0.01 mol%. The RLGA was calibrated using gas mixtures of known O_2 and CO concentrations to an accuracy of 0.02 mol %. Additional cycles were run for long-term durability testing in which the heating and cooling rates were unchanged, but the reduction time was shortened to 4 min, the oxidation time to 2.5 min, and the purge to 0.5 min. After cycling, the system was cooled to 500 °C at 200 °C min^{-1}, and then to 25 °C at 20 °C min^{-1}.

To identify the best fiber composition for stability and reactivity studies, parametric experiments for $Ce_{1-x}Zr_xO_2$ composition (with x = 0.0, 0.025, 0.05, 0.10) were carried out. The 2.5 mol% Zr composition ($Ce_{0.975}Zr_{0.025}O_2$) was selected for additional study because it achieved similar CO production rates to undoped ceria and retained a smaller crystallite size, indicative of improved resistance to sintering. The $Ce_{0.975}Zr_{0.025}O_2$ fibers were tested to evaluate the impact of the reduction temperature over the range of 1200 to 1500 °C on the reactivity and stability of the fiber microstructure. Finally, to assess the long-term stability of the $Ce_{0.975}Zr_{0.025}O_2$ fibers, 108 thermochemical cycles were completed over the course of 30 h at the preferred T_{red} of 1400 °C identified from the reduction temperature parametric experiments.

Results

In Figure 2a, an SEM image of a representative electrospun $Ce_{0.9}Zr_{0.1}O_2$ sample before testing demonstrates the non-woven textile appearance of the electrospun fiber structures. The fibers have a relatively narrow range of diameters, although a few fibers are bundled together to form a ‘yarn-like’ structure. The high-throughput, wire-coil spinneret in this study allows for the production of multiple fibers simultaneously, and fiber entanglement or bundling becomes

possible. High throughput spinning is desirable for large-scale production of such materials for fuel production cycles.

The SEM image of the untested $Ce_{0.9}Zr_{0.1}O_2$ fibers in Figure 2a shows some degree of pitting, which likely results from rapid solvent removal or polymer decomposition during initial processing. The features associated with pitting disappear after exposure to high temperatures due to grain growth and sintering along the fiber axis as shown by the SEM images in Figure 2b of fibers held at 1430 °C in air for 6 hours. Figure 2b shows how the small-diameter fibers densify through grain growth along the fiber axis. This illustrates how the non-woven fiber structures with their associated porosity maintain high amounts of separation and thereby inhibit grain growth. The grain growth in the electrospun fibers is substantially less than that of ~1 μm $Ce_{0.9}Zr_{0.1}O_2$ powders shown in Figure 2c exposed to the same high-temperature conditions. Such structural benefits make the Zr-doped ceria fibers an intriguing candidate for solar-driven fuel production in thermochemical redox cycles.

Initial redox cycling explored the impact of $Ce_{1-x}Zr_xO_2$ composition on CO production capacity and reoxidation kinetics with CO_2 with T_{red} approaching 1200 °C and with T_{ox} of 800 °C. Tests were carried out for 10 cycles and focused on the impact of relatively low Zr-dopant levels (with x = 0.0, 0.025, 0.05, 0.10). These tests were performed at lower T_{red} than typically desired for ceria-based materials to avoid any confounding effect of slow cyclical sintering observed at higher T_{red}. The average results after 10 redox cycles are summarized in Table 1. The data demonstrate a significant increase in ceria reduction yield with relatively small amounts of Zr doping. Even with a 60 °C lower T_{red}, $Ce_{0.975}Zr_{0.025}O_2$ provides more than twice the CO production capacity per g of material than that of undoped CeO_2. Increasing the Zr-doping further to 10% produces almost four times the CO production capacity of pure CeO_2.

However, consistent with prior studies [22, 24, 27], the increase in Zr from 0 to 10 mol% increases the time required to reoxidize the ceria from 20 to ~80 s as shown in Figure 3, which plots CO production rates of each composition vs. time for the 10th redox cycle. Favorable doping levels of $Ce_{0.975}Zr_{0.025}O_2$ and $Ce_{0.95}Zr_{0.05}O_2$ provide more than twice as much CO production as the undoped system after 10 cycles and reach complete oxidation in a reasonable time of approximately 40 s.

The value of low levels of Zr-doping is further illustrated in Figure 4, which shows XRD for the (222) ceria peaks as a function of Zr-doping after the 10 reduction cycles. The broadening of the (222) ceria peaks in Figure 4 with increased Zr-doping indicates that Zr-doping results in smaller crystallite sizes. Rietveld refinement of the XRD peaks was used to quantify this decrease in crystallite sizes with increased Zr-doping (Table 1). Crystallite sizes for the fibers after 10 redox cycles at a relatively low T_{red} of 1200 °C or less remain below 250 nm for pure CeO_2 and decrease down to 140 nm for $Ce_{0.9}Zr_{0.1}O_2$. Table 1 also shows how the shifts in peak location with increased Zr-doping as shown in Figure 4 correspond to a decrease in lattice parameters due to the smaller ionic radius of Zr^{4+} relative to Ce^{4+}. In general, the small amounts of Zr-doping considered here provide benefits of reduced sintering at 1200 °C and thus improved fiber ductility (with smaller crystallite sizes) and projected durability at higher temperatures for ceria-based redox cycling.

Based on the increased degree of reducibility and the relatively short time to reoxidize the ceria, the $Ce_{0.975}Zr_{0.025}O_2$ composition was chosen for an extensive study on the impact of increased T_{red} on reduction yields, oxidation kinetics, and evolution of surface area with cycling. The performance $Ce_{0.975}Zr_{0.025}O_2$ fiber samples were explored by experiments with T_{red} of 1200, 1300, 1400, and 1500 °C and a fixed T_{ox} = 800 °C. The transient CO production was measured

over at least 10 redox cycles for each T_{red} as illustrated in Figure 5. The peak and mean CO production rates are uniform within ± 10% for the first 10 cycles from cycle to cycle.

Figures 6a and 6b show instantaneous CO production rates and O_2 release rates respectively for the 10th cycle. In Figure 6a, the peak CO production rate at 800 °C increases from 7 to 17 and 45 mL min^{-1} g^{-1} as T_{red} is increased from 1200 to 1300 to 1400 °C. However, for T_{red} = 1500 °C, peak CO production rate decreases to 32 mL min^{-1} g^{-1}. Integrating the transient CO production rates over time provides a total CO production (on a mL g^{-1} basis), which is readily converted into a change in degree of reduction, Δδ. These results, as tabulated in Table 2, show that the total change in degree of reduction based on CO production increases monotonically with T_{red} up to 1500 °C even though peak CO production rates decline after exposure at 1500 °C.

The trends with T_{red} in peak reoxidation rates and total reoxidation are explained by looking at how the oxidation rate depends on fiber properties and the concentration of oxygen vacancies. The oxidation rate is a function of exposed surface area and fraction of exposed surface vacancies ($V_O^{\cdot\cdot}$) according to reaction R4.

$$V_O^{\cdot\cdot}\left(CeO_x\right) + CO_2\left(g\right) \leftrightarrow O_O^x\left(CeO_x\right) + CO\left(g\right) \qquad \text{(R4)}$$

The fraction of exposed surface vacancies will increase with overall δ, which increases with T_{red}, based on surface/bulk vacancy equilibrium. On the other hand, the exposed fiber specific surface area, a_{surf}, as found by BET analysis of Kr-absorption measurements after cycling, drops monotonically from 3.17 to 0.28 m^2 g^{-1} over the range from 1200 to 1500 °C (Table 2). The specific surface area decreases by slightly more than a factor of 2 for each 100 °C rise in T_{red}. This loss in surface area explains why the peak CO production rate is lower for T_{red} = 1500 °C even though the total integrated CO production is higher. The increase in vacancy

concentrations due to increased δ outweighs the loss in specific surface area until the highest T_{red} in this study.

In spite of the lowest surface area, the highest T_{red} provides the highest rates of O_2 release, as illustrated in Figure 6b, which shows the O_2 release rate for the 10th cycle during the ramp up to and the 5 min hold at T_{red}. In Figure 6b, time $t = 0$ starts at the beginning of the ramp from 800 °C in 10 ppm O_2. As such, the curves show that the O_2 release rate continuously increases with temperature during the ramp and is largely a function of temperature and not of surface area. Furthermore, the rate of O_2 release peaks when T_{red} is first reached because the reduction reaction (R5) is fast and thus in quasi-equilibrium with the surrounding gas phase.

$$2 \cdot O_O^x \left(CeO_x\right) \leftrightarrow 2 \cdot V_O^{\cdot\cdot} \left(CeO_x\right) + O_2\left(g\right) \qquad \text{(R5)}$$

This behavior of the O_2 release rate is consistent with previous studies on reduction of porous CeO_2 structures.[18] Oxygen continues to be released during the hold at T_{red} because the reduction proceeds non-uniformly in the bed. Oxygen released in the upstream regions of the 5-cm-long bed expose the downstream region of the bed to higher P_{O2} and thus conditions that favor less reduction. As the wave of reduction sweeps through the bed, the O_2 release rate decreases with time as less of the bed is participating in reduction. Because R5 is highly endothermic with an enthalpy of ~ 910 kJ gmol^{-1} for pure CeO_2 at $\delta = 0$ and of ~ 810 kJ gmol^{-1} for $\delta = 0.1$[41], the equilibrium favors O_2 production with increasing temperature. Since the reaction rate does not appear to be surface-limited like the oxidation reaction R4, higher T_{red} provides higher O_2 release rates. Nonetheless, because of the relatively low flow rates used in the current study, the time to sweep the released O_2 through the bed and drop the effective P_{O2} throughout the bed causes the average O_2 release rates to be much slower than the CO oxidation rates at T_{ox} as shown by

comparing rates in Figures 6a and 6b. The impact of the O_2 release on the reduction rates has significant impacts on operation and design of a reduction reactor.[42, 43]

In addition to the impact of T_{red} on loss of surface area, the effect of T_{red} on the general fiber structure is important for assessing robustness. To this end, SEM images of the post-cycled $Ce_{0.975}Zr_{0.025}O_2$ fiber samples were taken as shown in Figure 7 for each T_{red}. Figure 7 illustrates both the change in fiber structure and the loss in surface area with increasing T_{red}. At 1200 °C (Figure 7a), the fibers maintain the pitting formed in the synthesis process during the solvent evaporation/polymer decomposition step. The pitted nature of the fibers sustains a relatively high surface area of 3.17 m^2 g^{-1} (Table 2). After reduction at 1300 °C (Figure 7b), the fibers retain some degree of pitting but the pits are fewer and smaller due to sintering which decreased surface area to 1.54 m^2 g^{-1}.

Further increase in T_{red} to 1400 °C (Figure 7c) results in further decrease in surface area of the $Ce_{0.975}Zr_{0.025}O_2$ fibers to 0.60 m^2 g^{-1}. The morphology of the fibers changes due to significant grain growth along the fiber axis. The grain growth results in collapse of the pitted structure, but as shown in Figure 6a, the loss of surface area does not cause a loss in peak CO production during reoxidation. At T_{red} = 1500 °C, the $Ce_{0.975}Zr_{0.025}O_2$ fibers agglomerate as shown in the SEM image in Figure 7d. The agglomeration leads to a reduction in surface area to 0.28 m^2 g^{-1}, which slows the rate of CO production. The inset plot in Figure 6a indicates that the time to complete reoxidation for T_{red} = 1500 °C is greater than the 4 min hold at 800 °C and 25% CO_2, while at T_{red} = 1400 °C, the samples appear to be fully reoxidized in approximately 2 min. The slow oxidation with the low 2.5% Zr-doping may limit the change in δ for redox cycles with very high T_{red} and practically limited times of exposure at these temperatures. A recent study on redox cycles of Zr- and Hf-doped CeO_2 powders indicates that after reduction at 1500 °C and

substantial particle sintering, reoxidation was not complete in 40 vol% CO_2 at 800 °C after 25 min.[22] Even though the fiber structures in this study show a loss of surface area at 1500 °C, the nature of sintering along the fiber axis does not result in the loss of surface area that leads to the long reoxidation times seen with less sinter-resistant powders.

Long-term Cycling Survey

To assess the long-term viability of the $Ce_{0.975}Zr_{0.025}O_2$ electrospun fibers, a fiber sample was cycled over the course of 30 h with T_{red} and T_{ox} nominally set to 1400 °C and 800 °C, respectively. Long-term cycling provides a measure of how evolution of the fiber structure influences cyclic CO production. Figure 8a shows the cyclic variation of the fiber temperature, the rates of production of CO during oxidation and release of O_2 during reduction over the 108 cycles. Figure 8a shows that the peak CO production rate drops from around 30 mL min^{-1} g^{-1} in the first few cycles to a relatively steady rate between 13 and 14 mL min^{-1} g^{-1} after 60 cycles. This decrease is explained by the loss in the fiber specific surface area from 0.60 m^2 g^{-1} after 10 cycles to 0.34 m^2 g^{-1} after 100 cycles (Table 2). Stabilization in peak CO production rate for the final 50+ cycles indicates that the fiber microstructure stabilized with little further change in specific surface area. Figure 8a also shows the O_2 release rates, which have far smaller and broader peaks spread out over the temperature ramp and hold at T_{red}. Although not clear from Figure 8a, the O_2 release rates also stabilize after approximately 60 cycles, and thus, the cycles occurring near the end of this experiment may represent the long-term, stable performance of $Ce_{0.975}Zr_{0.025}O_2$ electrospun fibers undergoing redox cycle with T_{red} of 1400 °C and T_{ox} around 800 °C.

Figure 8b shows the time-integrated CO production and O_2 release per cycle for the long-term cycling tests. As expected by stoichiometry, the total O_2 release for each cycle is close to

50% of the cyclic CO production, although the low signal to noise ratio in the long tails of the O_2 release rate (as exemplified earlier by Figure 6b) limit the accuracy of the integrated O_2 release over the full reduction period. The measurement of CO production is more accurate, and the observed increase in total CO production from 3.2 to 4.0 mL/g over the 100+ cycles occurs even while the fiber surface area is decreasing. This 20-25% increase in CO production is attributed to the slight rise in reduction temperature in the fiber bed from 1390 °C to 1405 °C over the 108 cycles. The slight increase in peak temperature leads in turn to higher CO production capacity due to the high sensitivity of chemical equilibrium of the endothermic O_2 release with temperature. Although thermodynamic data for $Ce_{0.975}Zr_{0.025}O_2$ are not available in the scientific literature, the rise in production is consistent with the equilibrium thermodynamics of undoped CeO_2. For $P_{O2} = 10^{-5}$ atm, the measured temperature change would raise the reduction non-stoichiometry by 0.0035 for pure ceria based on equilibrium δ for undoped ceria from previous studies[12], and such an increase in δ would correspond to an increase of 0.8 mL g^{-1} of CO produced for $Ce_{0.975}Zr_{0.025}O_2$.

Figure 9 shows SEM images of $Ce_{0.975}Zr_{0.025}O_2$ electrospun fibers after the long-term cycling. After 108 cycles with T_{red} at 1400 °C, the fibers exhibit 'bead-like' structures indicative of further grain growth even while maintaining a highly porous overall structure. The relatively high surface area of the fibers after cycling allows them to reach 90% reoxidation (based on the detection limit of the gas analyzer) in less than 70 s even as shown in Figure 9. The finding that Zr-doped ceria fibers maintain relatively fast oxidation over so many redox cycles with relatively high total CO production suggests their potential for possible implementation in large-scale CO production processes. Rapid rates of reduction and oxidation over sustained cycling are key indicators for reaching meaningful solar-to-fuel efficiencies for the ceria cycle because relatively

small swings in non-stoichiometry between reduction and oxidation require rapid cycling. Moreover, prior analyses of process thermodynamic efficiency point to the advantage of using short duration reduction and oxidation times to achieve higher average production rates while minimizing the use of excess oxidant and sweep gas.[9, 18, 43]

Conclusions

Electrospun ceria-based fibers offer significant potential for as a low cost, high surface area material structure for solar thermochemical metal-oxide redox cycles to convert concentrated solar energy to fuel. The promise of ceria fibers lightly doped with zirconia ($Ce_{1-x}Zr_xO_2$ where x = 0.0, 0.025, 0.05, 0.10) has been demonstrated by thermochemical cycling in a rapid heating IR furnace coupled with extensive material characterization by scanning electron microscopy, X-ray diffraction, and Kr physisorption. The $Ce_{0.975}Zr_{0.025}O_2$ fibers were selected among the doping options because in short term cycles this composition increased CO production without sacrificing the rate of production. Moreover, the fibers maintain high surface area after exposure to reduction temperatures as high as 1400 °C.

Cycling the $Ce_{0.975}Zr_{0.025}O_2$ fibers between reduction at 1400 °C and oxidation at 800 °C over 30 h in 108 cycles demonstrates the promise of the fibers for thermochemical fuel production. The $Ce_{0.975}Zr_{0.025}O_2$ samples retain the fiber morphology and surface areas of ca. 0.3 $m^2\ g^{-1}$, higher than post-testing surface areas of other structured ceria-based materials for solar thermal cycling. The stability of the fiber structure gives rise to stable and favorable rates of CO production,and the present study suggests that electrospun fibers are capable of sustaining peak CO production rates of 13 mL $min^{-1}\ g^{-1}$ and an average rate of fuel production of 3.2 mL $min^{-1}\ g^{-1}$, twice the average rate demonstrated by alternative fuel production substrates. Implementing

steps to retain surface area will further enhance fuel production rates, particularly as reactor cycle time is decreased or reactor operation tends toward isothermal conditions. We conclude that Zr-doped ceria fibers have proven significant potential for implementation in solar reactors for thermochemical cycling of ceria to produce CO and by extension to H_2, via water splitting.

Acknowledgements

William Gibbons acknowledges the support of the John and Maureen Hendricks Charitable Foundation Energy Research Fellowship to support this work. The funding of the University of Minnesota Initiative for Renewable Energy and the Environment is appreciated. The University of Maryland's Nanocenter NISP lab provided the electron microscopy facilities, and Dr. Peter Zavalij in Chemistry and Biochemistry at the University of Maryland provided valuable assistance in performing the XRD measurements. The authors would also like to acknowledge University of Minnesota students Aayan Banerjee and Peter T. Krenzke who helped with the long-term thermochemical cycling tests.

References

1. G. P. Smestad and A. Steinfeld, *Ind. Eng. Chem. Res.*, 2012, **51**, 11828-11840.
2. C. Perkins, P. R. Lichty and A. W. Weimer, *Intl. J. Hydrogen Energ.*, 2008, **33**, 499-510.
3. L. J. Venstrom and J. H. Davidson, *J. Sol. Energ.-Trans. ASME*, 2011, **133**, #011017.
4. S. Abanades, *Intl. J. Hydrogen Energ.*, 2012, **37**, 8223-8231.
5. J. R. Scheffe, J. H. Li and A. W. Weimer, *Intl. J. Hydrogen Energ.*, 2010, **35**, 3333-3340.
6. J. R. Scheffe, A. H. McDaniel, M. D. Allendorf and A. W. Weimer, *Energ. Environ. Sci.*, 2013, **6**, 963-973.
7. W. C. Chueh and S. M. Haile, *Philos. Trans. Roy. Soc. A*, 2010, **368**, 3269-3294.
8. S. Abanades, A. Legal, A. Cordier, G. Peraudeau, G. Flamant and A. Julbe, *J. Mater. Sci.*, 2010, **45**, 4163-4173.
9. P. Furler, J. R. Scheffe and A. Steinfeld, *Energ. Environ. Sci.*, 2012, **5**, 6098-6103.
10. M. Romero and A. Steinfeld, *Energ. Environ. Sci.*, 2012, **5**, 9234-9245.
11. M. Mogensen, N. M. Sammes and G. A. Tompsett, *Solid State Ionics*, 2000, **129**, 63-94.
12. R. J. Panlener, R. N. Blumenthal and J. E. Garnier, *J. Phys. Chem. Solids*, 1975, **36**, 1213-1222.
13. O. T. Sørensen, *J. Solid State Chem.*, 1976, **18**, 217-233.
14. J. R. Scheffe and A. Steinfeld, *Energ. Fuel.*, 2012, **26**, 1928-1936.
15. S. G. Rudisill, L. J. Venstrom, N. D. Petkovich, T. T. Quan, N. Hein, D. B. Boman, J. H. Davidson and A. Stein, *J. Phys. Chem. C*, 2013, **117**, 1692-1700.
16. L. J. Venstrom, N. Petkovich, S. Rudisill, A. Stein and J. H. Davidson, *J. Sol. Energ.-Trans. ASME*, 2012, **134**, #011005.
17. W. C. Chueh, C. Falter, M. Abbott, D. Scipio, P. Furler, S. M. Haile and A. Steinfeld, *Science*, 2010, **330**, 1797-1801.
18. P. Furler, J. Scheffe, M. Gorbar, L. Moes, U. Vogt and A. Steinfeld, *Energ. Fuel.*, 2012, **26**, 7051-7059.
19. H. Kaneko, S. Taku and Y. Tamaura, *Sol. Energ.*, 2011, **85**, 2321-2330.
20. N. D. Petkovich, S. G. Rudisill, L. J. Venstrom, D. B. Boman, J. H. Davidson and A. Stein, *J. Phys. Chem. C*, 2011, **115**, 21022-21033.
21. A. Le Gal and S. Abanades, *J. Phys. Chem. C*, 2012, **116**, 13516-13523.
22. J. R. Scheffe, R. Jacot, G. R. Patzke and A. Steinfeld, *J. Phys. Chem. C*, 2013, **117**, 24104-24114.
23. C. I. Lee, Q. L. Meng, H. Kaneko and Y. Tamaura, *J. Sol. Energ.-Trans. ASME*, 2013, **135**, #011002.
24. Q. L. Meng, C. I. Lee, H. Kaneko and Y. Tamaura, *Thermochim. Acta*, 2012, **532**, 134-138.
25. S. Abanades and A. Le Gal, *Fuel*, 2012, **102**, 180-186.
26. A. Le Gal and S. Abanades, *J. Phys. Chem. C*, 2012, **116**, 13516-13523.
27. A. Le Gal and S. Abanades, *Intl. J. Hydrogen Energ.*, 2011, **36**, 4739-4748.
28. Q.-L. Meng, C.-i. Lee, H. Kaneko and Y. Tamaura, *Thermochim. Acta*, 2012, **532**, 134-138.
29. Q.-L. Meng, C.-i. Lee, S. Shigeta, H. Kaneko and Y. Tamaura, *J. Solid State Chem.*, 2012, **194**, 343-351.
30. H. Kaneko, T. Miura, H. Ishihara, S. Taku, T. Yokoyama, H. Nakajima and Y. Tamaura, *Energy*, 2007, **32**, 656-663.

31. G. Balducci, M. S. Islam, J. Kaspar, P. Fornasiero and M. Graziani, *Chem. Mater.*, 2000, **12**, 677-681.
32. R. Ruiz-Rosas, J. Bedia, J. M. Rosas, M. Lallave, I. G. Loscertales, J. Rodríguez-Mirasol and T. Cordero, *Catal. Today*, 2012, **187**, 77-87.
33. W. T. Gibbons, T. H. Liu, K. J. Gaskell and G. S. Jackson, *Appl. Catal. B-Environ.*, 2014, **in review for publication**.
34. K. M. Forward and G. C. Rutledge, *Chem. Eng. J.*, 2012, **183**, 492-503.
35. N. M. Tikekar and J. J. Lannutti, *Ceram. Intl.*, 2012, **38**, 4057-4064.
36. S. Brunauer, P. H. Emmett and E. Teller, *J. Amer. Chem. Soc.*, 1938, **60**, 309-319.
37. H. S. Gandhi, G. W. Graham and R. W. McCabe, *J. Catal.*, 2003, **216**, 433-442.
38. J. Kašpar, P. Fornasiero and N. Hickey, *Catal. Today*, 2003, **77**, 419-449.
39. E. Mamontov, T. Egami, R. Brezny, M. Koranne and S. Tyagi, *J. Phys. Chem. B*, 2000, **104**, 11110-11116.
40. L. Vegard, *Z. Physik*, 1921, **5**, 17-26.
41. M. Zinkevich, D. Djurovic and F. Aldinger, *Solid State Ionics*, 2006, **177**, 989-1001.
42. D. J. Keene, W. Lipinski and J. H. Davidson, *Chem. Eng. Sci.*, 2014, **accepted for publication**.
43. L. J. Venstrom, R. M. De Smith, Y. Hao, S. M. Haile and J. H. Davidson, *Energ. Fuel.*, 2014, **accepted for publication**.

Table 1. Fuel production as a function of dopant concentration for un-doped and doped CeO_2 samples. Post-cycling XRD indicates that lattice parameter and crystallite size decrease with increased Zr content (determined via Rietveld refinement of XRD).

Sample	T_{red} (°C)	T_{ox} (°C)	V_{CO} (mL g^{-1})	$\Delta\delta$ ($\times 10^3$)	Lattice parameter (Å)	Crystallite size (nm)
CeO_2	1200	800	0.40 ± 0.05	2.8 ± 0.3	5.4111	234.3
$Ce_{0.975}Zr_{0.025}O_2$	1140	760	0.98 ± 0.06	6.9 ± 0.7	5.4047	194.3
$Ce_{0.95}Zr_{0.05}O_2$	1130	760	0.90 ± 0.10	6.5 ± 0.7	5.3988	176.3
$Ce_{0.90}Zr_{0.10}O_2$	1140	740	1.60 ± 0.10	12.0 ± 0.1	5.3833	140.5

Table 2. Surface areas (measured via Kr adsorption) from the $Ce_{0.975}Zr_{0.025}O_2$ reduction temperature survey experiments as well as the long term cycling with all BET fits having R^2-value > 0.9998

T_{red} (°C)	Number of cycles	Final V_{CO} (mL g^{-1})	$\Delta\delta$	BET a_{surf} (m^2/g)	a_{surf} error +/- (m^2/g)
1200	10	0.88	0.006	3.17	0.13
1300	10	1.6	0.011	1.54	0.07
1400	10	4.7	0.033	0.60	0.03
1500	10	7.0*	0.049	0.28	0.02
1400	100	3.9*	0.027	0.34	0.02

Figure Captions

Figure 1. Fiber production via electrospinning set-up: (a) wire coil spinneret which is rotated through a bath of spinning solution, fibers are collected on a rotating wire drum collector, (b) removal of the collected fibers from the wire drum leaves a non-woven mat of polymer & ceramic precursor fibers, (c) SEM of the ceramic + precursor fibers shows the high degree of uniformity of the as-spun fiber materials.

Figure 2. Fiber structure advantage with respect to temperature stability for $Ce_{0.90}Zr_{0.10}O_2$ fibers and powders. Fibers following polymer removal (heating to 550 °C in air) (a), fibers after heating to 1430 °C in air for 6 hours (b), and a powder sample for comparison subjected to the same heating cycle as the fibers.

Figure 3. CO production rates at T_{ox} = 800 °C with 25% CO_2 inlet flows for different $Ce_{1-x}Zr_xO_2$ fiber samples with varying x = 0.0, 0.025, 0.05, and 0.1. The rates are plotted for the 10^{th} redox cycle for the relatively low T_{red} listed in Table 1.

Figure 4. XRD for the samples of $Ce_{1-x}Zr_xO_2$ for x = 0.0, 0.025, 0.05, and 0.1 after 10 redox cycles as described in Table 1. The lattice parameter varies linearly with Zr content as expected by Vegard's Law. With increasing Zr content, diffraction peaks shift to higher angles 2Θ and peaks undergo broadening.

Figure 5. CO production rates at T_{ox} = 800 °C with 25% CO_2 inlet flows for 10 redox cycles of $Ce_{0.975}Zr_{0.025}O_2$ using different T_{red} (1200-1500 °C). Peak rates and total fuel production increases as T_{red} is raised from 1200-1400 °C.

Figure 6. a) CO production rates vs. time for the 10^{th} cycle for $Ce_{0.975}Zr_{0.025}O_2$ fibers for different T_{red}. Inset plot shows the final 3 minutes of the CO production step for the samples reduced with T_{red} = 1400 °C and 1500 °C, and indicates that the sample reduced at 1500 °C may not return to equilibrium in the time provided for oxidation. b) O_2 production rate vs. time for the 10^{th} cycle for $Ce_{0.975}Zr_{0.025}O_2$ fibers for different T_{red} . The plot shows O_2 production during both the temperature ramp to T_{red} and the hold at T_{red}. Time is zeroed at the beginning of the ramp from 800 °C up to T_{red}.

Figure 7. Scanning electron microscopy images of tested $Ce_{0.975}Zr_{0.025}O_2$ temperature survey samples, (a) T_{red} = 1200°C and sample shows limited sintering with many bundled fibers produced when fibers become entangled while leaving the spinneret, (b) T_{red} = 1300°C produces relatively limited sintering with bundled fibers still showing some pore-like contact points, (c) T_{red} = 1400 °C leads to high degree of sintering in which bundled fibers have melded together to form larger diameter fibers and the pore-like features have been eliminated, (d) T_{red} = 1500 °C shows even further sintering but fiber structure is still discernable.

Figure 8. Temperature, CO production rates, and O_2 release rates for $Ce_{0.975}Zr_{0.025}O_2$ fiber sample during 108 complete redox cycles with T_{red} = 1400 °C. The CO production rate in blue shows the sharp peak at the beginning of the re-oxidation step which decays asymptotically with

increasing cycle number due to fiber sintering and loss of surface area. The O_2 release rate during high-temperature in red has a relatively small and broad peak that is spread out over the period of heating to and holding at T_{red}. b) Cycle variation in total time-integrated CO production and O_2 release (in mL g^{-1}) and in maximum reduction temperature for the $Ce_{0.975}Zr_{0.025}O_2$ sample measured over the 108 cycles with T_{red} = 1400 °C.

Figure 9. Scanning electron microscopy images (1, 2, 5, 10kX magnification for images a,b,c,d) of $Ce_{0.975}Zr_{0.025}O_2$ following the long-term stability test with T_{red} = 1400°C. After 100+ cycles the fiber structure is partially retained.

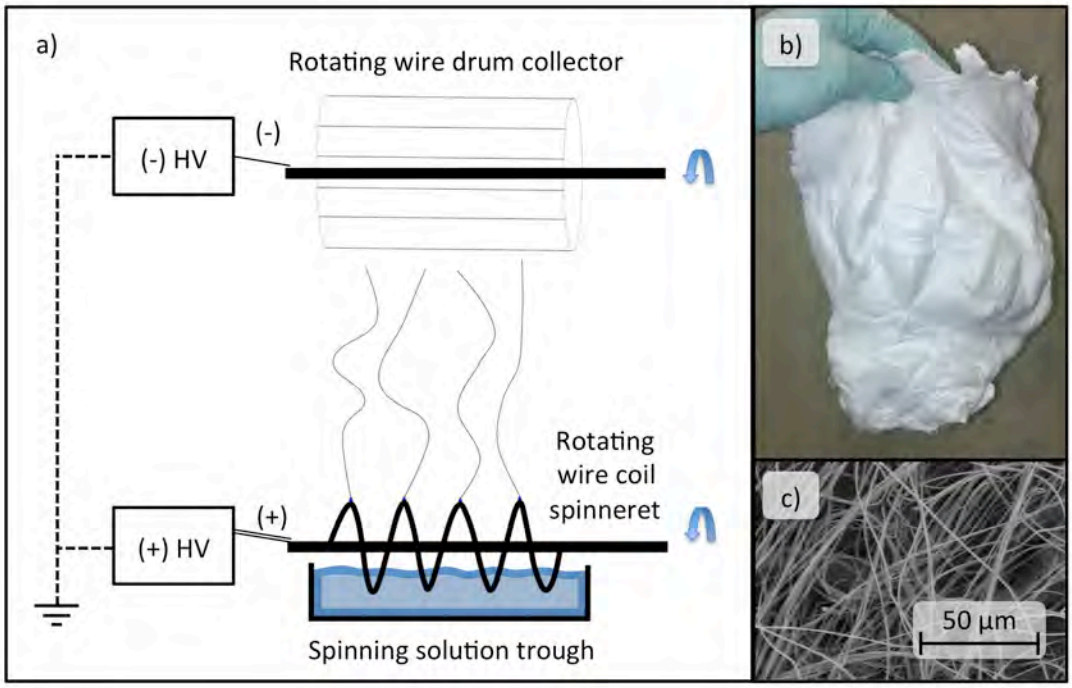

FIGURE 1

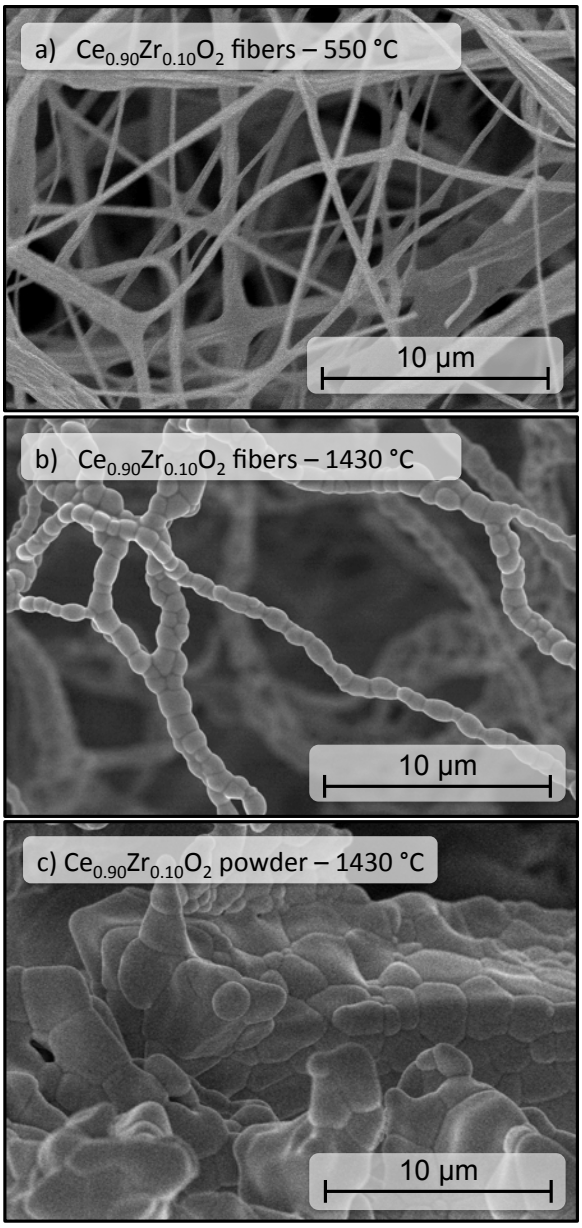

FIGURE 2

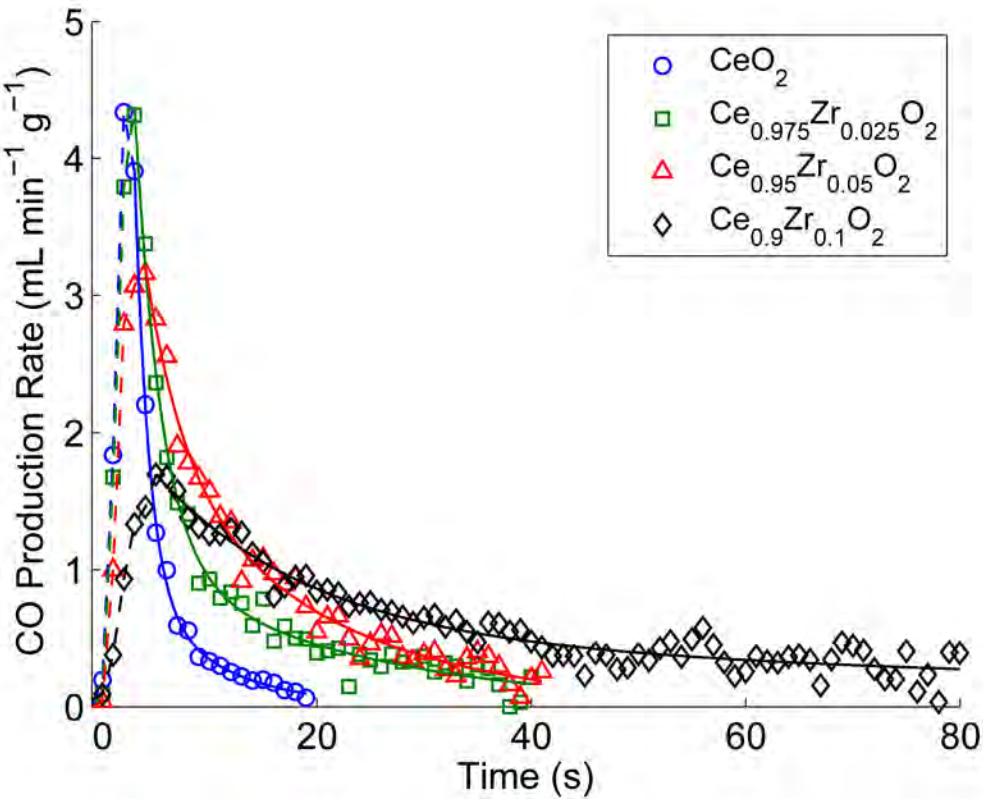

FIGURE 3

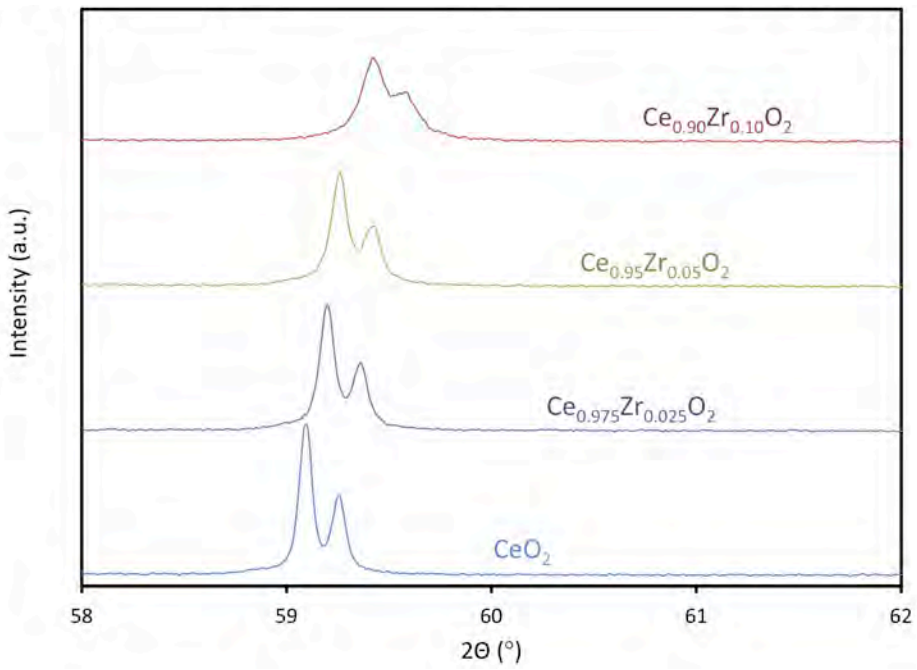

FIGURE 4

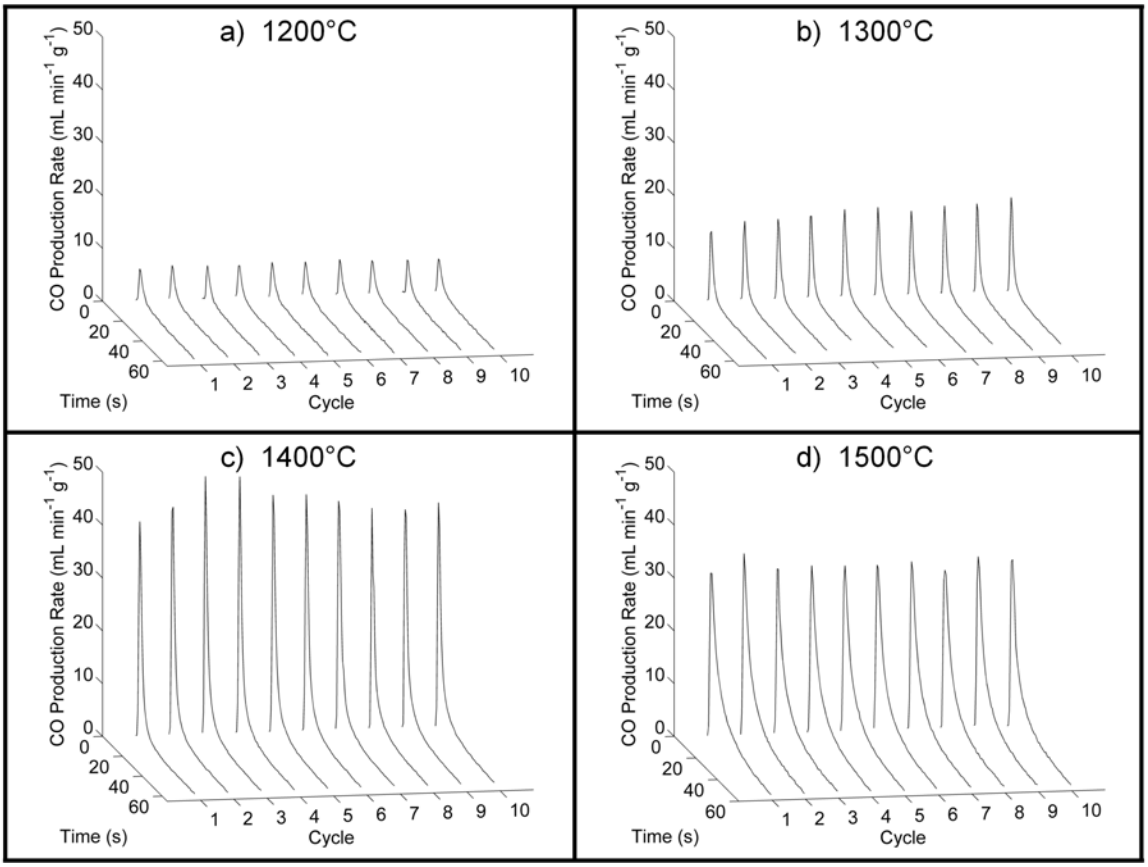

FIGURE 5

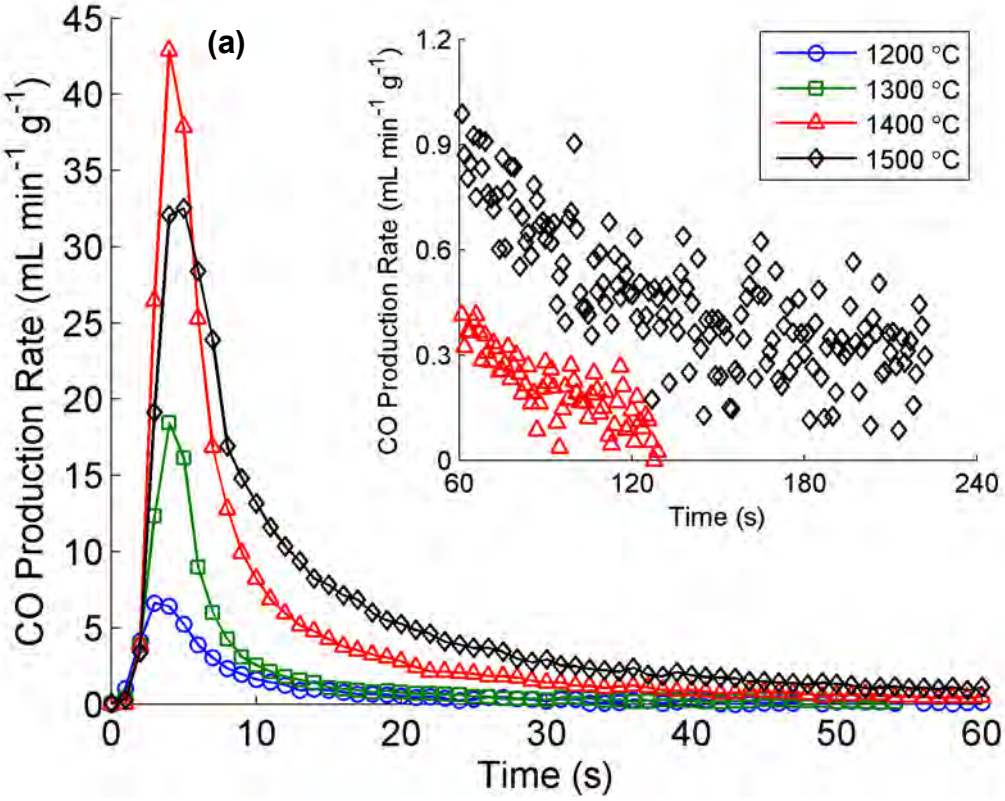

FIGURE 6a

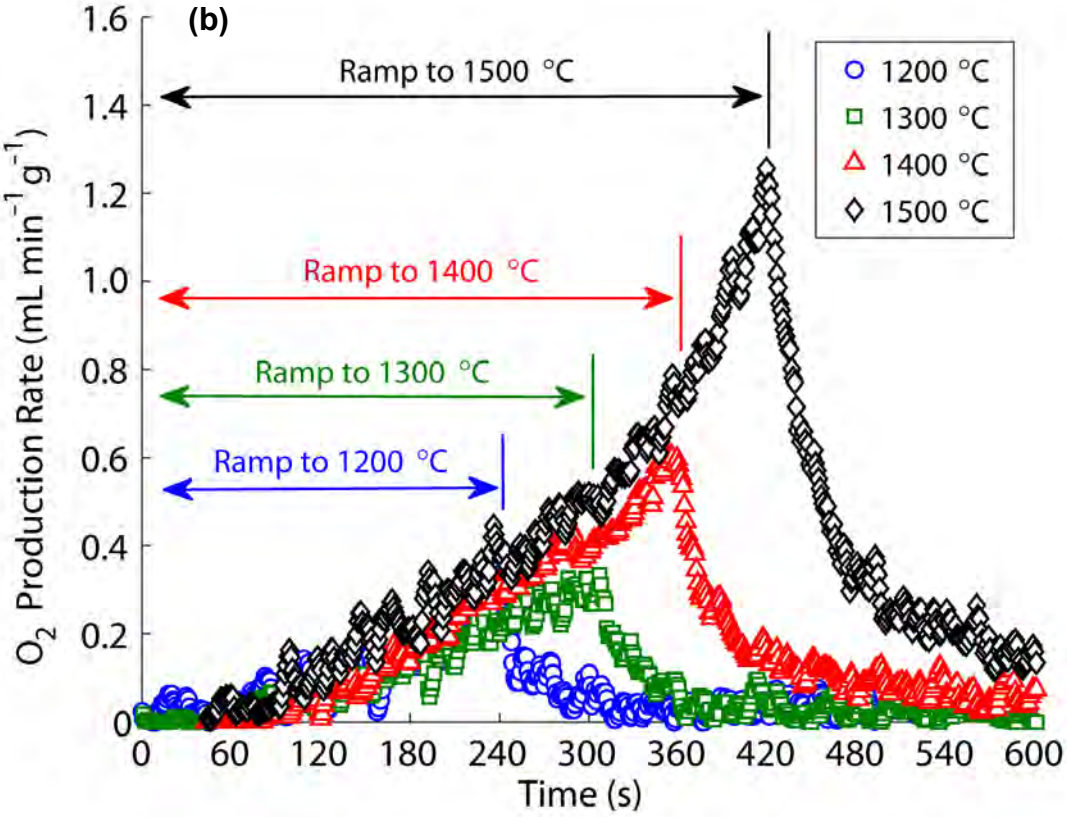

FIGURE 6b

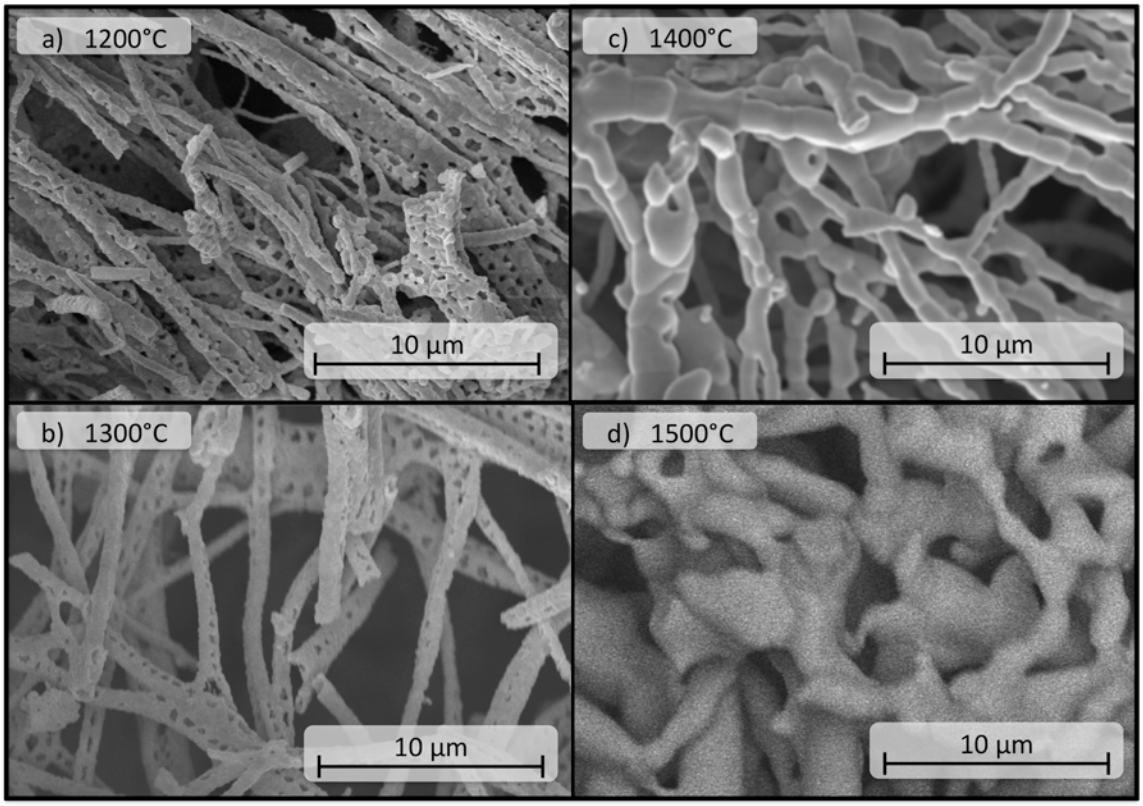

FIGURE 7

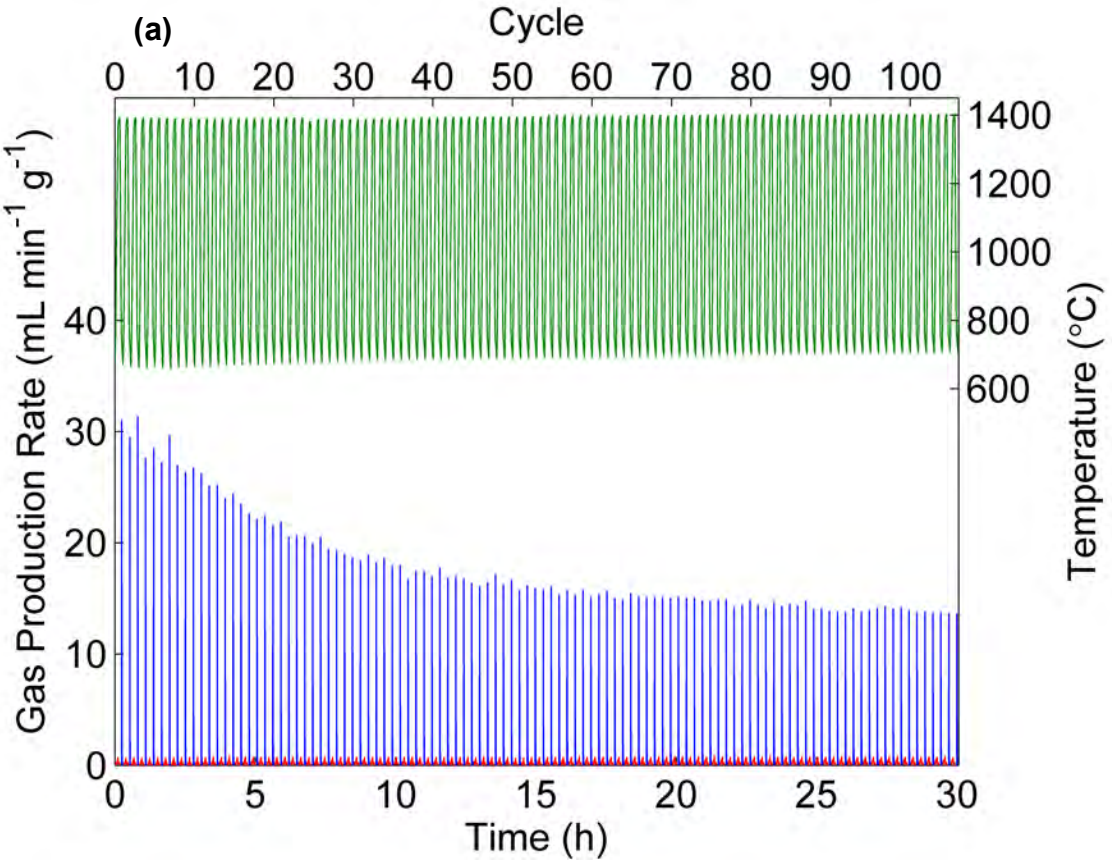

FIGURE 8a

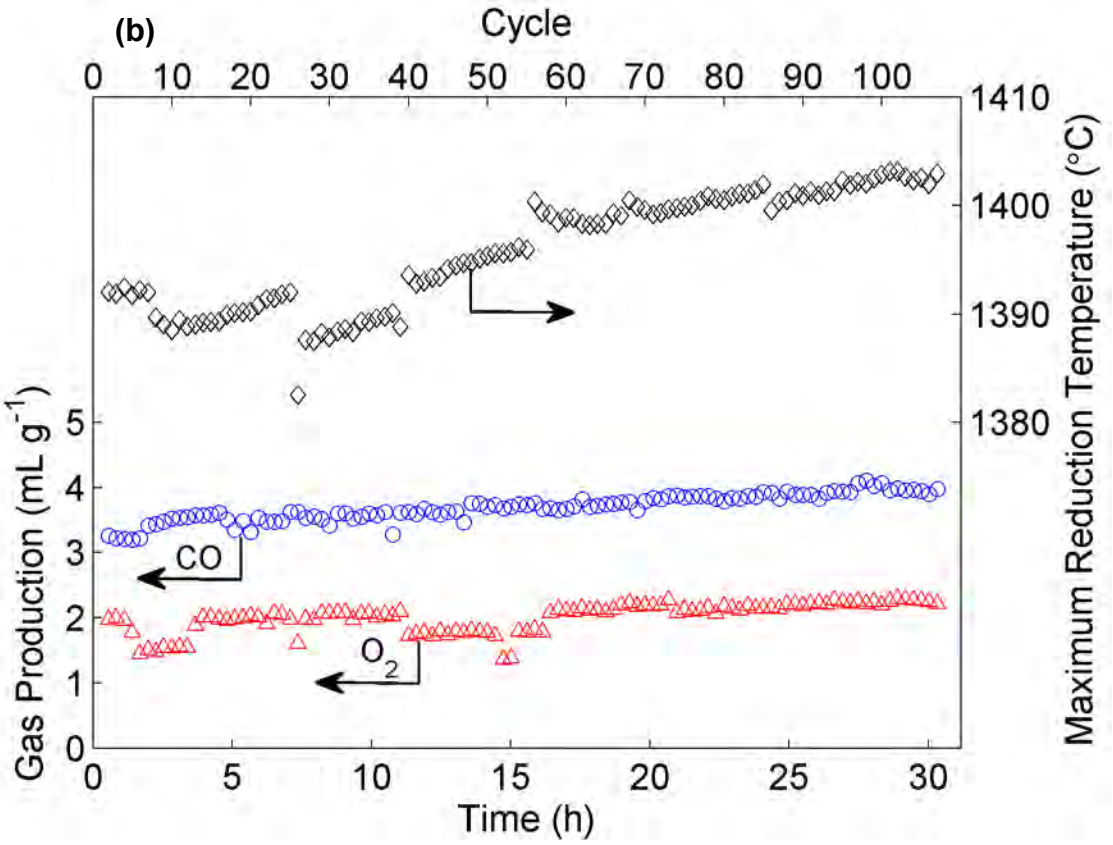

FIGURE 8b

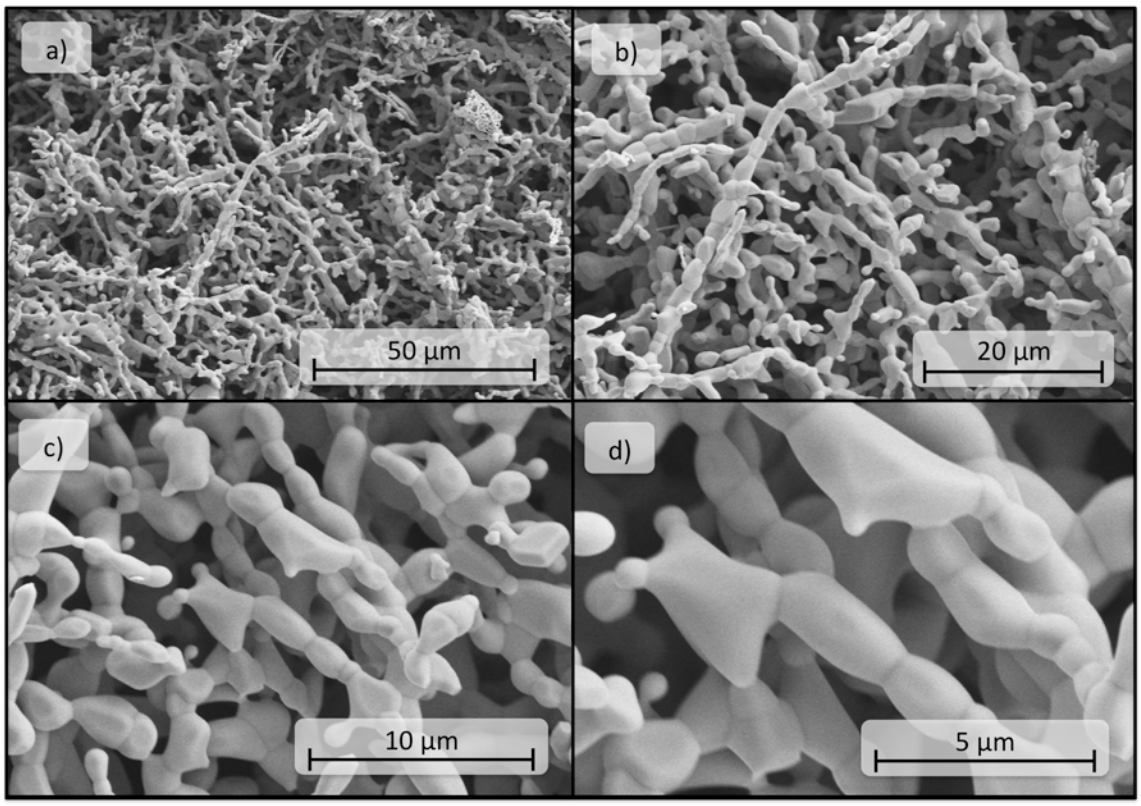

FIGURE 9

Graphical Abstract for

Ceria-based Electrospun Fibers for Renewable Fuel Production via Two-Step Thermal Redox Cycles for Carbon Dioxide Splitting

by William T. Gibbons, Luke J. Venstrom, Robert M. De Smith, Jane H. Davidson, and Gregory S. Jackson